JACS
JOURNAL OF THE AMERICAN CHEMICAL SOCIETY

pubs.acs.org/JACS

Article

Influence of Defects and H_2O on the Hydrogenation of CO_2 to Methanol over Pt Nanoparticles in UiO-67 Metal–Organic Framework

Emil Sebastian Gutterød, Sri Harsha Pulumati, Gurpreet Kaur, Andrea Lazzarini, Bjørn Gading Solemsli, Anette Eleonora Gunnæs, Christian Ahoba-Sam, Maria Evangelou Kalyva, Johnny Andreas Sannes, Stian Svelle, Egill Skúlason, Ainara Nova,* and Unni Olsbye*

Cite This: *J. Am. Chem. Soc.* 2020, 142, 17105–17118

Read Online

ACCESS | Metrics & More | Article Recommendations | Supporting Information

ABSTRACT: In catalysts for CO_2 hydrogenation, the interface between metal nanoparticles (NPs) and the support material is of high importance for the activity and reaction selectivity. In Pt NP-containing UiO Zr-metal–organic frameworks (MOFs), key intermediates in methanol formation are adsorbed at open Zr-sites at the Pt–MOF interface. In this study, we investigate the dynamic role of the Zr-node and the influence of H_2O on the CO_2 hydrogenation reaction at 170 °C, through steady state and transient isotope exchange experiments, H_2O cofeed measurements, and density functional theory (DFT) calculations. The study revealed that an increased number of Zr-node defects increase the formation rates to both methanol and methane. Transient experiments linked the increase to a higher number of surface intermediates for both products. Experiments involving either dehydrated or prehydrated Zr-nodes showed higher methanol and methane formation rates over the dehydrated Zr-node. Transient experiments suggested that the difference is related to competitive adsorption between methanol and water. DFT calculations and microkinetic modeling support this conclusion and give further insight into the equilibria involved in the competitive adsorption process. The calculations revealed weaker adsorption of methanol in defective or dehydrated nodes, in agreement with the larger gas phase concentration of methanol observed experimentally. The microkinetic model shows that $[Zr_2(\mu\text{-}O)_2]^{4+}$ and $[Zr_2(\mu\text{–}OH)(\mu\text{-}O)(OH)(H_2O)]^{4+}$ are the main surface species when the concentration of water is lower than the number of defect sites. Lastly, although addition of water was found to promote methanol desorption, water does not change the methanol steady state reaction rate, while it has a substantial inhibiting effect on CH_4 formation. These results indicate that water can be used to increase the reaction selectivity to methanol and encourages further detailed investigations of the catalyst system.

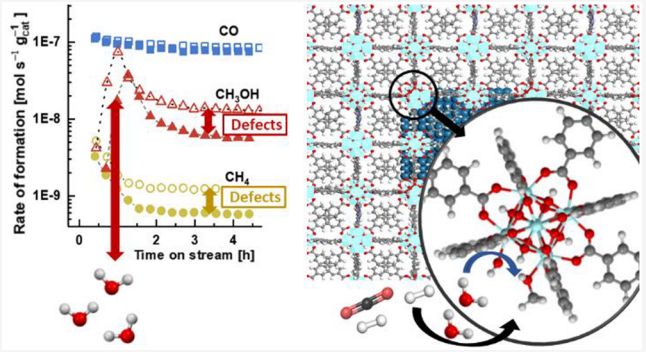

INTRODUCTION

The hydrogenation of CO_2 is receiving attention as a key reaction for sustainable production of fuels and value-added chemicals.[1−3] The activity and selectivity of CO_2 hydrogenation catalysts is strongly influenced by the nature of the metal–support interface.[4−8] For Cu-based catalysts, the presence of ZrO_2 or isolated Zr moieties close to Cu facilitates methanol formation by forming low coordinated Lewis acidic Zr-sites, where formate and methoxy groups form in the presence of CO_2 and H_2.[9−11] Formate and methoxy groups are also observed at sites at the interface of Cu/Al_2O_3: at 4-coordinated sites, methanol forms from bidentate CO_2 bridged between two sites, via formate, while at 3-coordinated sites, CO formation from monodentate CO_2 is favored.[12] On Pt/Al_2O_3, it has been proposed that CO forms from carbonate-type intermediates on defective Al sites at the interface, either by O-abstraction by hydrogen, or by the filling of an oxygen vacancy.[13]

Studies of the CO_2 hydrogenation reaction to methanol over metal functionalized metal–organic frameworks (MOFs) have also brought further evidence of interactions between the nanoparticles (NPs) and the support material.[14−18] Focusing here on the UiO-series of MOFs, they consist of 12-coordinated $Zr_6O_4(OH)_4^{12+}$ nodes connected by, e.g., benzene-1,4-dicarboxylic acid linkers (BDC; UiO-66) or biphenyl-4,4′-dicarboxylic

Received: July 3, 2020
Published: September 9, 2020

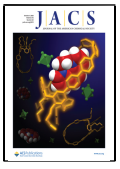

acid linkers (BPDC; UiO-67), forming 3-dimensional, porous frameworks with fcc structure.

X-ray photoelectron spectroscopy (XPS) performed on Cu NPs at the UiO-66 surface showed evidence of Zr reduction in the presence of Cu, suggesting an interaction between the Cu NPs and the UiO-66 Zr-node.[14] Furthermore, An et al. reported XPS evidence of Zr reduction in CuZn@UiO-67 with 100% bipyridine type linkers, and proposed that the reaction proceeds by CO_2 adsorption at unsaturated Zr-sites followed by H-spillover from Cu to the Zr-node.[15]

In two recent contributions from our group, we reported the CO_2 hydrogenation performance of an exceptionally stable MOF-based catalyst, consisting of Pt nanoparticles (NPs) in situ formed in the cavities of UiO-67, herein called "UiO-67-Pt". The first contribution focused on stability issues,[16] while the second focused on catalyst performance and mechanistic studies.[17] A performance comparison was carried out between UiO-67-Pt and Pt/C, Pt/SiO_2 and Pt/Al_2O_3 catalysts. The study showed that Pt/C and Pt/SiO_2 produced only CO, while Pt/Al_2O_3 produced mainly CO and a modest amount of methane and methanol (<10% selectivity to each of methane and methanol) at 170 °C, 1−8 bar, H_2/CO_2 = 6. Notably, UiO-67-Pt formed substantial amounts of methanol (up to 18% selectivity), smaller amounts of methane (up to 2% selectivity), and CO as the majority product, under the same conditions. Combining steady state and transient kinetic methods revealed that methanol is formed from CO_2 via formate intermediates at open Zr-sites at the interface between the Pt NP and the Zr-node. The study further showed that methanol is mechanistically separated from the byproducts, methane and CO, and that methane is formed mainly via CO, on this catalyst.[17]

In the current study, the focus is set on the dynamic role of the Zr-node in UiO-67-Pt during the CO_2 hydrogenation reaction. We investigate the influence of the amount of defective open Zr-sites (i.e., sites not coordinated to linker molecules) on the formation of all three carbon-containing reaction products: methanol, methane, and CO. Moreover, we employ steady state and transient water cofeed experiments, involving isotope labeling and DFT calculations, to gain insight into the role of node-hydration and influence of water in the reaction. The study shows a positive correlation between the number of node defects and the number of surface intermediates leading to methanol and methane formation, while it has a minor influence on CO formation. Furthermore, water cofeed was found to promote desorption of methanol, while it is detrimental to the formation of methane. These findings provide important leads to further catalyst and process design.

EXPERIMENTAL SECTION

The sample of UiO-67 was prepared by the procedure reported in ref 17: in brief, a solution of $ZrCl_4$ (1 equiv), distilled water (6 equiv), and dimethylformamide (DMF) (50 equiv) was heated to 80 °C, and benzoic acid (3 equiv) was added. When the benzoic acid (BA) was dissolved, 2,2′-bipyridine-5,5′-dicarboxylic acid (BPYDC) (0.1 equiv) and 1,1′-biphenyl-4,4′-dicarboxylic acid (BPDC) (0.9 equiv) were added, and the resulting solution was heated under stirring overnight at 130 °C. The resulting MOF was washed with hot DMF and acetone, and then dried overnight (in air) at 150 °C. This sample is referred to as UiO-67.

To produce a sample with less missing linker defects, a BPDC healing procedure (modified from literature)[19] was performed: 5 g of the UiO-67 sample, predried at 200 °C was dispersed in 100 mL DMF at 100 °C. BPDC (0.6 g) was added to the solution to replace the BA in UiO-67 (12.5% with respect to BPDC, vide infra) with BPDC. After heating the solution at 100 °C overnight, the resulting powder was washed with DMF and acetone as above. This sample is referred to as UiO-67(LD).

Both MOF samples were impregnated with Pt following the procedure reported in ref 16: K_2PtCl_4 corresponding to a 2:1 BPYDC:Pt molar ratio was added to the MOFs dispersed in DMF at 100 °C under stirring and left overnight. After washing in hot DMF and acetone, this leads to the formation of well-defined BPYDC-$PtCl_2$ moieties (where the BPYDC is in the MOF framework).[20,21]

For Pt/ZrO_2, ZrO_2 particles were prepared by a modified literature procedure.[22] 2.15 g of $ZrO(NO_3)_2{\cdot}xH_2O$ (99%, supplied by Sigma-Aldrich) was dissolved in 100 mL type 2 water and heated to 70 °C under reflux, followed by a dropwise addition of 100 mL of 0.3 M $(NH_4)_2CO_3$ (ACS Reag. Ph. Eur grade, from Merk KGaA) aqueous solution under stirring. After 2 h of stirring, the resulting mixture was cooled to ambient temperature, centrifuged, and then washed twice with type 2 H_2O. The resulting paste was oven-dried at 110 °C for 12 h and then calcined in air at 500 °C for 3 h. The calcined ZrO_2 was impregnated with 0.5 wt % Pt following the same procedure as for the MOF samples. Powder X-ray diffractograms of the MOFs were acquired using a Bruker D8 Discover instrument (Cu Kα) with a Lynx Eye silicon detector. N_2 adsorption isotherms were measured at 77 K (BELSORP mini-II) after heating the samples under vacuum for 1 h at 80 °C then 4 h at 150 °C. After dissolving the samples in 1 M NaOH/D_2O, solution state proton nuclear magnetic resonance (^{1}H NMR) was utilized to determine the relative amounts of organic species in the MOFs. Thermogravimetric analysis was performed on a Netzsch STA 449 F3-Jupiter instrument. The samples (~20 mg) were heated to 800 °C in an Al_2O_3 sample holder under flow of 20 mL min^{-1} 20% O_2/N_2. A Hitachi SU8230 field emission scanning electron microscope (FESEM) with an XFlash 6l10 energy-dispersive X-ray (EDX) detector was used to estimate the Pt/Zr ratio of the two samples. The Pt/Zr ratio in the two samples were equal within the experimental accuracy (0.042 ± 0.002 and 0.043 ± 0.003 for UiO-67-Pt and UiO-67(LD)-Pt, respectively). Scanning transmission electron microscopy (STEM) images of UiO-67(LD)-Pt after activation and testing was acquired with a FEI Titan G2 60−300 kV microscope.

Most catalytic tests were performed in a fixed bed flow test setup with a stainless-steel reactor (I.D. 7 mm) where the effluent gas is analyzed by an online MS (Pfeiffer) and a GC (TCD-FID). Prior to catalytic testing, the materials were activated at 350 °C (5 °C min^{-1} ramp and 4 h isotherm) in flow of 10% H_2/Ar (40 mL min^{-1}). The catalysts (0.2 g) were tested in 1/3/1 and 1/6/3 CO_2/H_2/Ar flow (τ = 0.01, g_{cat} min mL^{-1}) under 1 and 8 bar pressure, at 170 °C. Prehydration, H_2O cofeed, and $^{13}CO_2/^{12}CO_2$ SSITKA (Steady-State Isotope Transient Kinetic Analysis) experiments were performed and the details are reported in-text.

The high-pressure catalytic tests were performed using a Microactivity Effi unit built by PID Eng & Tech (Micromeritics). The unit is equipped with a high-speed servo-controlled needle valve which allows for precise and stable control of pressure from 1 to 100 bar. A stainless steel flow reactor (6 mm I.D) was used for the tests. The catalysts were activated at 350 °C (5 °C/min ramp) for 4 h in 10% H_2 in inert (10% Kr in Ar) flow prior to the testing. The catalysts (0.2 g) were tested with 1/6/3 CO_2/H_2/inert flow ratios (τ = 0.01 and 0.02 g_{cat} min mL^{-1} for the UiO-67-Pt and Pt/ZrO_2 samples, respectively) aimed at similar CO_2 conversions within 1−30 bar, and 170−240 °C. The effluent from the reactor was analyzed with an online GC (Agilent 8890 equipped with one TCD and 2 FIDs, with a methanizer coupled to one of the FIDs to analyze both CO_x and oxygenates on one column using one detector).

Computational Details. For the computational study, all chemical species were optimized using DFT calculations with a mixed Gaussian and plane wave method (GPW),[23−25] as implemented in CP2K-6.1 version.[26,27] We used PBE-D3 functional[28,29] with Gaussian basis set DZVP-MOLOPT-SR-GTH.[30,31] A multigrid of size 5 was used to map the Gaussian basis functions, with cutoff energy of 360 Ry for plane wave basis. Energy barriers were calculated using the climbing image nudged elastic band (CI-NEB) method.[32,33] The microkinetic model is built with COPASI.[34] Further details on the calculations are given in the Supporting Information (SI).

https://dx.doi.org/10.1021/jacs.0c07153
J. Am. Chem. Soc. 2020, 142, 17105−17118

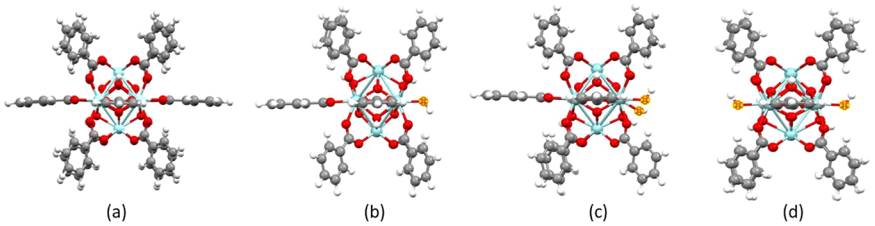

Figure 1. (a) Zirconium node with 12 benzoate linkers. (b) A defective node is created by removing one linker resulting in a Zr-node with 11 linkers. (c) A defective node with two adjacent missing linkers. (d) A defective node with two opposite missing linkers. The carbon atoms furthest away from the Zr-node were constrained in all cases in all directions, to simulate the integrity of the UiO-67 MOF.

In our previous study[17] we concluded that the active site for methanol formation are the Zr-nodes of the UiO-67 system. In this work, the reactivity of the Zr-sites active toward the reaction products CH_3OH and H_2O, was explored in more detail. To decrease the computational cost of the overall study, we constructed a simple model where the UiO-67 framework optimized from our previous work[17] is stripped to a single zirconium node with 12 benzoate linkers, as shown in Figure 1(a). To maintain the structure of the MOF and better simulate the real configuration of the catalyst, carbon atoms at the end of the linkers were constrained in all directions to prevent the node from deforming and maintaining the integrity of the MOF. One linker was removed from the model in Figure 1(a) to simulate a missing linker defect as shown in Figure 1(b). This system is used to investigate the equilibrium between methanol and water desorption. Two linkers were also removed from the original 12 linkers model system to create either the two adjacent missing linker defects in Figure 1(c) or two opposite missing linker defects in Figure 1(d). The one linker and two linker defect systems were used to model the UiO-67(LD) and the UiO-67 systems, respectively (Figure 2). This model should sufficiently replicate the qualitative aspects of the catalytic system. Missing linker defects may be capped by OH^-/H_2O molecules.[17,35−37]

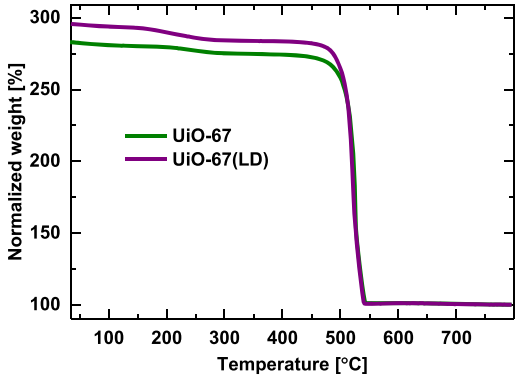

Figure 2. Thermogravimetric analysis of UiO-67 (green) and UiO-67(LD) (purple). The materials were heated at 5 °C min^{-1} to 800 °C in 25 mL min^{-1} 20% O_2/N_2.

With the DFT calculated energetics we constructed a micro kinetic model (MKM) that represents all possible chemical reactions for methanol and water adsorption and desorption. To study the role of water in the transient formation of methanol we performed an isotope study by replacing hydrogen with deuterium in all intermediates and built another MKM as shown in SI Figure S13.

RESULTS AND DISCUSSION

Characterization. XRD and N_2 adsorption of UiO-67 before and after the BPYDC healing procedure, called UiO-67 and UiO-67(LD), respectively, showed that the procedure had no effect on the crystallinity of the MOF, nor any significant effect on the porosity and surface area of the material (SI Figures S1 and S2). This finding suggests that the structural change of the system, if any, is minor.

In line with previous studies of the material, solution state ^{1}H NMR analysis identified four organic carboxylate species in both samples; BPDC, BPYDC, benzoic acid (BA), and formic acid (FA), where formic acid originates from decomposition of DMF during synthesis (SI Figure S3).[38] Quantification of the relative amounts of the species, with respect to BPDC showed that the BPYDC amount was comparable in the two samples, and in good agreement with the target amount of synthesis (11 and 10% in UiO-67 and UiO-67(LD), respectively) (Table 1). The benzoic acid amount was 60% lower in the UiO-67(LD) sample. Thus, successful replacement of a major portion of the benzoic acid in the UiO-67 sample was achieved through the BPDC healing procedure. A minor amount of FA (2%) was observed in both samples.

Table 1. Solution State ^{1}H-NMR Data of UiO-67 and UiO-67(LD)[a]

sample	BPYDC	benzoic acid (BA)	formic acid (FA)
UiO-67	11	12.5	2.0
UiO-67(LD)	9.9	4.8	1.8

[a]The amounts are given as percent with respect to BPDC.

Both materials show the same TGA-decomposition profile, but the normalized weight predecomposition (T < 500 °C) is significantly higher in the BPDC-healed analog UiO-67(LD), evidencing that the number of Zr-sites coordinated to linker or benzoate is higher as compared to the pristine UiO-67 sample.

Defect calculations[39] were performed by combining the results from ^{1}H NMR and evaluating the normalized weight during TGA at 200 °C. They showed that BPDC-healing procedure resulted in an increased BPDC/node ratio (increasing from 4.75 to 5.35) and a decreased BA/node ratio (0.68 to 0.27), while the BPYDC and FA to node ratios were unchanged (Table 2). Thus, the parent MOF UiO-67 has, after synthesis, on average one less linker coordinated to each Zr-node, as compared to the healed analog.[40] This translates into one

Table 2. Defectivity of UiO-67 before and after the BPDC Healing Procedure, Estimated from Solution State ^{1}H-NMR and TGA[a]

sample	wt $\%_{200\ °C}$	BPDC	BPYDC	BA	FA
UiO-67	279	4.75	0.59	0.68	0.1
UiO-67(LD)	290	5.35	0.58	0.27	0.1

[a]The values for each species are per Zr-node. (BPDC+BPYDC): Zr-node (cluster) = 6 in the perfect UiO-67 system, each node being coordinated to 12 carboxylate groups.

https://dx.doi.org/10.1021/jacs.0c07153
J. Am. Chem. Soc. 2020, 142, 17105−17118

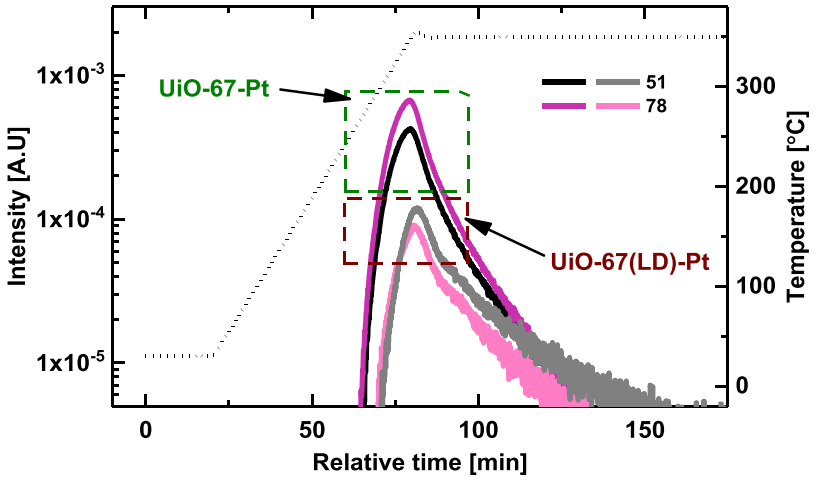

Figure 3. Online MS signals related to benzoate/linker type fragments during activation of UiO-67-Pt (lilac/black) and UiO-67(LD)-Pt (pink/gray). Conditions: 5 °C min^{-1} ramp to 350 °C (4 h dwell) in 20 mL (min·0.1 g_{cat}) $^{-1}$ flow of 10% H_2/Ar.

potential active site for methanol formation per node at the Pt-MOF interface,[17] or a total of 660 and 70 μmol open Zr sites per gram of UiO-67 or UiO-67(LD) material, respectively.

In our previous work on the UiO-67-Pt material, species originating from benzoate/linkers, as well as residual DMF solvent, were observed in gas phase during the activation procedure at 350 °C in 10% H_2/Ar.[17] Figure 3 shows the two most intense online MS signals related to benzoate/linker type fragments during activation of UiO-67-Pt and UiO-67(LD)-Pt. The same signal profile is observed for both materials; however, in line with the TGA and ^{1}H NMR results, a lower amount of benzoate related species is released from the BPDC-healed sample, UiO-67(LD)-Pt.

TEM images of UiO-67(LD)-Pt after activation at 350 °C (4 h) followed by testing for CO_2 hydrogenation at 170 °C for ~4.5 h (vide infra) are shown in Figure 4. The size of the Pt NPs is

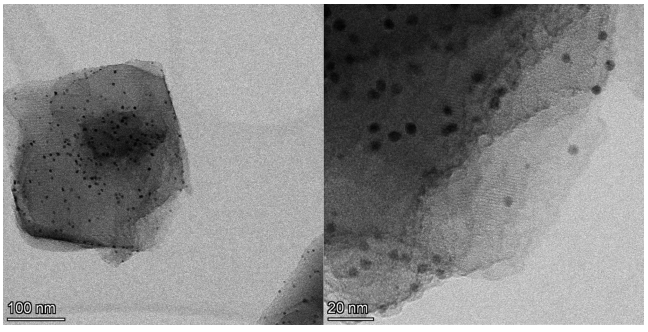

Figure 4. Bright field STEM images of UiO-67(LD)-Pt after activation followed by reaction-onset testing (vide infra). See SI for instrument details.

around 4 nm in diameter (3.9 ± 0.6 nm), which is comparable to the nonhealed UiO-67-Pt analog (3.6 ± 0.7 nm, see ref 17). Thus, the two catalysts are comparable both in Pt amount and NP size, but differ in the number of Zr node defects, and are therefore suited for investigating the influence of defects on the CO_2 hydrogenation reaction.

An XPS study was carried out for UiO-67 (with 10% bipy linkers) before and after Pt impregnation, and after subsequent reductive pretreatment as well as catalytic testing (SI Figures S5–S7). The study showed that Pt is mainly in reduced state, and that Zr(IV) is partly reduced to Zr(III), after reduction and after subsequent testing of UiO-67-Pt. The results are in agreement with previous XAS studies of UiO-67-Pt and with XPS and NAP-XPS studies of Cu/UiO-66 and CuZn/UiO-67.[14−17]

CO_2 adsorption isotherms were measured at 25−50 °C for pristine UiO-67 and for UiO-67-Pt before and after reduction (SI Figure S8). Pt impregnation and subsequent reduction led to a small reduction in CO_2 uptake per gram material, but did not change the measured interaction strength between CO_2 and the material. The CO_2 adsorption enthalpy was in all cases 18−19 kJ/mol, similar to what previously reported for UiO-67 MOF.[41]

Catalytic Investigation. *UiO-67-Pt versus Pt/ZrO_2.* Conversion-selectivity plots versus pressure and temperature for UiO-67-Pt and Pt/ZrO_2, obtained under steady-state conditions, clearly demonstrate the superior methanol production ability of the MOF-based catalyst, with a maximum of 42% (versus 6%) methanol selectivity at 30 bar, 170−190 °C, at similar conversion (Figure 5). This result confirms the unique metal−support interaction created between Pt NPs stabilized by the UiO-67 framework, and the defect (linker-deficient) Zr-nodes surrounding it. The methanol selectivity observed for the Pt/ZrO_2 catalyst is similar to what was previously reported, i.e.; 6% methanol selectivity at 200 °C, 10 atm.[22]

Influence of Missing Linker Defects on the Reaction. The influence of missing linker defects in UiO-67 (UiO-67-Pt versus UiO-67(LD)-Pt) on catalytic performance was evaluated in a "reaction-onset" experiment by the following procedure: First, the materials were activated in a reducing flow of 10% H_2 in Ar (40 mL min^{-1}, m_{cat} = 0.2 g, 1 bar) ramping to 350 °C followed by a 4 h isotherm before cooling to 170 °C in Ar flow. Second, the reaction feed of CO_2/H_2/Ar(10Kr) = 1/3/1, τ = 0.01 g_{cat} min mL^{-1} was introduced to the reactor and the reactor pressure was subsequently increased to 8 bar. The results are presented in Figure 6, where the formation rates of CO, CH_4, and CH_3OH are shown in the left-hand figure, and the CH_3OH selectivity is shown to the right.

Both catalysts show the same trends with time on stream: the rate of methanol formation increases rapidly during the first hour of reaction, then decreases comparatively fast and reaches a steady state after approximately 3 h on stream. At peak methanol formation, the rate is approximately 6 times higher than at steady state. The formation rates of CO and CH_4 both decrease with

https://dx.doi.org/10.1021/jacs.0c07153
J. Am. Chem. Soc. 2020, 142, 17105−17118

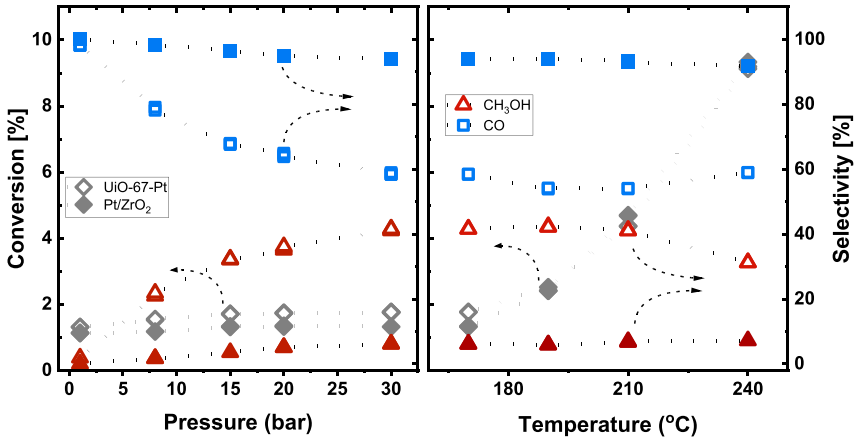

Figure 5. CO_2 conversion (left axes) and product selectivity (right axes) under varying pressure (left graph, T = 170 °C) and temperature (right graph, P_{tot} = 30 bar) conditions over UiO-67-Pt (open symbols) and Pt/ZrO_2 (filled symbols). CO_2 conversion (diamond), CO (square), and CH_3OH (triangle) selectivity. For brevity, the residual selectivity (<10%) to methane over UiO-67-Pt is not shown. Conditions: CO_2/H_2/inert = 1/6/2, τ = 0.01 $g_{uio\text{-}67\text{-}Pt}$ min mL^{-1}, 0.02 $g_{Pt/ZrO2}$ min mL^{-1}.

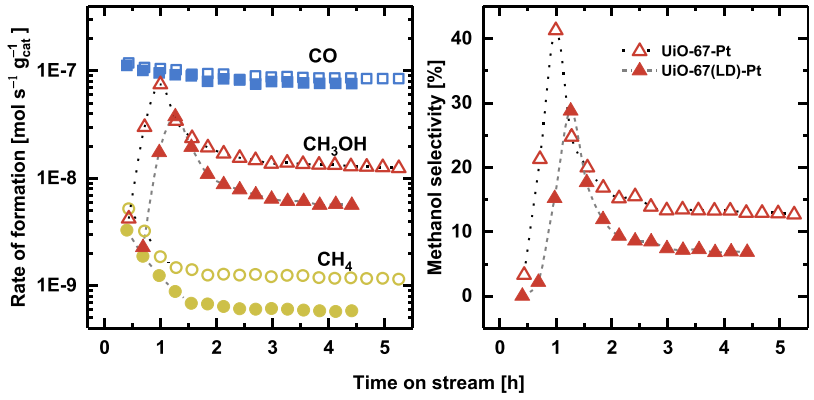

Figure 6. Reaction-onset comparison of UiO-67-Pt (open symbols) and UiO-67(LD)-Pt having intrinsically less benzoic acid modulator (filled symbols). Left: CO (squares), CH_3OH (triangles), and CH_4 (circles) rate of formation. Right: methanol selectivity versus time on stream. Conditions: CO_2/H_2/inert = 1/3/1, τ = 0.01 g_{cat} min ml^{-1}, T = 170 °C, 8 bar.

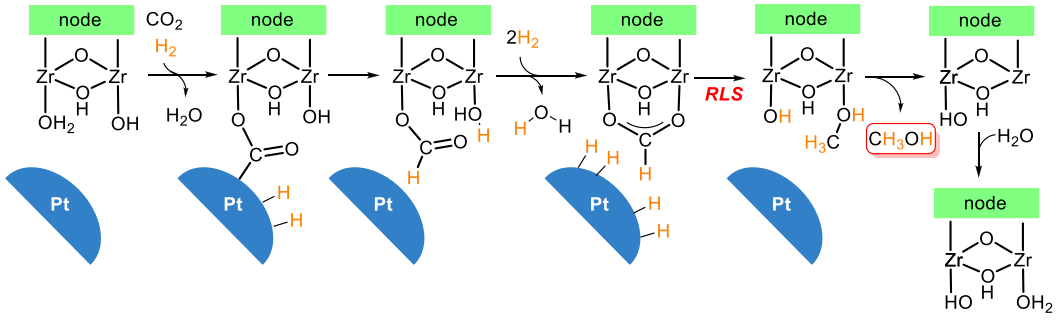

Figure 7. Postulated mechanism for methanol formation on an open Zr-site at the UiO-67-Pt Zr-node.

time on stream until steady state is reached after about 1.5 h. The relative temporal change is significantly larger for the small amounts of CH_4 formed, as compared to the majority product CO. Under the given conditions, the CH_4 selectivity was <1%. In a second experiment for UiO-67-Pt, where the tested sample was reactivated and retested, an identical transient behavior was observed (SI Figure S9), suggesting that the transient regime with decreasing activity is caused by reversible catalyst changes. The transient regime of the CO_2 hydrogenation reaction is addressed further in the next section.

Comparing the absolute values of the reaction rates over the two catalyst samples, it is evident that the CO formation rates are comparable, while the rate of methanol formation is approximately 60% lower (at steady state) over the less defective UiO-67(LD)-Pt sample (Figure 6). This corresponds to methanol selectivity of ~7% and ~13%, respectively. A 60% decrease was also observed in the methane formation rate, between the UiO-67 and UiO-67(LD) samples. To assess the reproducibility of the measurements, another identical test of UiO-67(LD)-Pt was performed. In that case, the same trend was observed and the methanol formation rate was somewhat higher,

https://dx.doi.org/10.1021/jacs.0c07153
J. Am. Chem. Soc. 2020, 142, 17105−17118

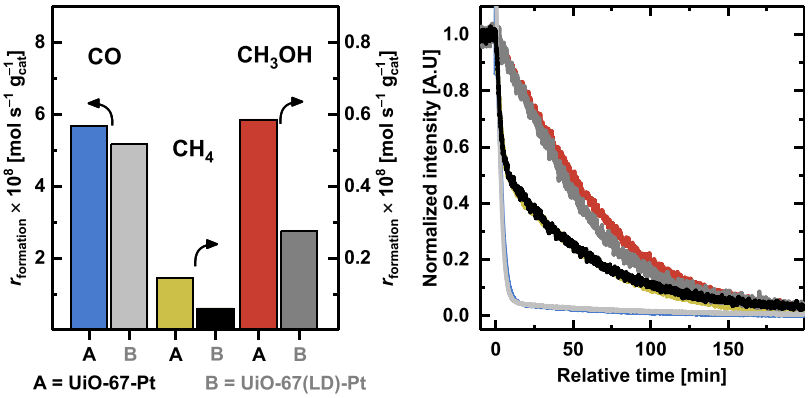

Figure 8. Left: Steady state reaction rates of ^{13}CO (blue, light gray), $^{13}CD_4$ (yellow, black), and $^{13}CD_3OD$ (red, dark gray) over UiO-67-Pt (A, colors) and UiO-67(LD)-Pt (B, gray tones). Right: Transient evolution of the ^{13}C-labeled products after switching from $^{13}CO_2$+D_2 to $^{12}CO_2$+D_2 at time = 0. ^{13}CO, $^{13}CD_4$, and $^{13}CD_3OD$ are represented by m/z = 29, 21 and 35, respectively. Conditions: CO_2/D_2/inert = 1/6/3, τ = 0.01 g_{cat} min mL^{-1}, T = 170 °C, 1 bar.

Table 3. Mean Surface Residence Times τ_{res} and Number N_{ad} of Surface Intermediates Leading to the Formation of ^{13}CO, $^{13}CD_4$, and $^{13}CD_3OD$ at 170 °C (1 bar), Calculated from Integration of the Curves and the Isotope-Independent Steady-State Reaction Rates in Figure 8[a]

	INT(CO)		INT(CD_4)		INT(CD_3OD)	
	τ_{res}	N_{ads}	τ_{res}	N_{ads}	τ_{res}	N_{ads}
UiO-67-Pt	0.5×10^3	26 ± 3	2.1×10^3	3 ± 0.3	3.8×10^3	23 ± 2
UiO-67(LD)-Pt	0.4×10^3	20 ± 3	2.0×10^3	1 ± 0.2	3.3×10^3	9 ± 1

[a]Values of τ_{res} are in seconds, and N_{ads} in μmol g_{cat}^{-1}.

yielding a selectivity of ~9% at steady state, while the methane formation rate was the same in both tests (SI Figure S10). The significantly lower activity toward methanol and methane formation over the less defective UiO-67(LD)-Pt sample strongly suggests that a lower number of defects leads to a lower number of active sites for both methanol and methane formation, in turn resulting in a lower rate of formation. This finding is perfectly in line with the postulated mechanism of methanol formation via a formate intermediate bound to open Zr-sites in the Pt NP−MOF interface (see Figure 7).[17] It further suggests that methane is also formed at the interface of the Zr-node and the Pt NP. Conversely, the similar CO formation rates observed over the two materials suggest that the rate-limiting step of CO formation is catalyzed by the Pt NP surface, without an influence of the Pt NP−Zr node interface.

To verify that the origin of the lower methanol and methane formation rates is the number of intermediates, we turned to $^{13}CO_2$ SSITKA measurements. Due to limitations in the transient experimental setup, the measurements were performed under ambient pressure. Moreover, the reaction was performed in D_2 instead of H_2 to increase the methanol production (caused by the strong inverse kinetic isotope effect)[17,42] and to allow for monitoring of both methanol and methane during the isotope transient. At steady state conditions (CO_2/D_2/inert = 1/6/3, τ = 0.01 g_{cat} min mL^{-1}, T = 170 °C, 1 bar), the rates of CO, methane, and methanol formation were approximately 10%, 60%, and 50% lower, respectively, over UiO-67(LD)-Pt than over UiO-67-Pt (Figure 8, left), comparable to the differences observed in experiments under 8 bar pressure. The transient evolution of ^{13}CO, $^{13}CD_4$ and $^{13}CD_3OD$ after switching from a feed of $^{13}CO_2$+D_2 to $^{12}CO_2$+D_2 at time = 0, is shown in Figure 8 (right). The transient evolution of the normalized intensity of the ^{13}C products formed over UiO-67(LD)-Pt overlap those of UiO-67-Pt, previously reported in ref 17, evidencing that the reaction proceeds through the same mechanism, with the same intrinsic kinetics, while the number of active sites is different.

The mean surface residence time τ_{res} and the number of surface intermediates N_{ad} leading to formation of the three products, listed in Table 3, are parameters where no underlying assumptions about the kinetic model is required.[43,44] In agreement with the overlapping isotope transients and the lower steady state methanol formation rate over UiO-67(LD)-Pt (50% of the rate over UiO-67-Pt), the number of intermediates leading to methanol formation on UiO-67(LD)-Pt is 40% of the number of intermediates on the defective analog. That is, $N_{ad,UiO\text{-}67(LD)\text{-}Pt}/N_{ad,UiO\text{-}67\text{-}Pt}$ = 0.4. A similar observation is made for methane formation, where $N_{ad,UiO\text{-}67(LD)\text{-}Pt}/N_{ad,UiO\text{-}67\text{-}Pt}$ = 0.3. These data confirm the importance of Zr-node defects for methane formation. N_{ad} for CO is, however, somewhat lower than expected for the defective analog, since similar reaction rates were observed over the two materials at 8 bar pressure, and only 10% lower CO formation rate was observed here. However, considering the error margins of the experiments and the data treatment, the agreement is reasonable.

As a final observation from the data presented in Figure 8 (right), it is interesting to note that the normalized methanol transients over UiO-67-Pt and UiO-67(LD)-Pt are very similar, in spite of the much higher total number of open Zr sites in UiO-67 (660 μmol/g) than in UiO-67(LD) (70 μmol/g). This observation suggests that readsorption of methanol on open Zr sites downstream of its formation site is kinetically irrelevant.

Influence of Zr-Node Hydration on the Reaction. In the comparison of UiO-67-Pt and UiO-67(LD)-Pt, after the onset of reaction at 8 bar pressure, a transient regime lasting approximately 2 h was observed for the formation of all three carbon-containing reaction products (see Figure 6). In this section, the origin of this transient regime is investigated for UiO-67-Pt.

https://dx.doi.org/10.1021/jacs.0c07153
J. Am. Chem. Soc. 2020, 142, 17105−17118

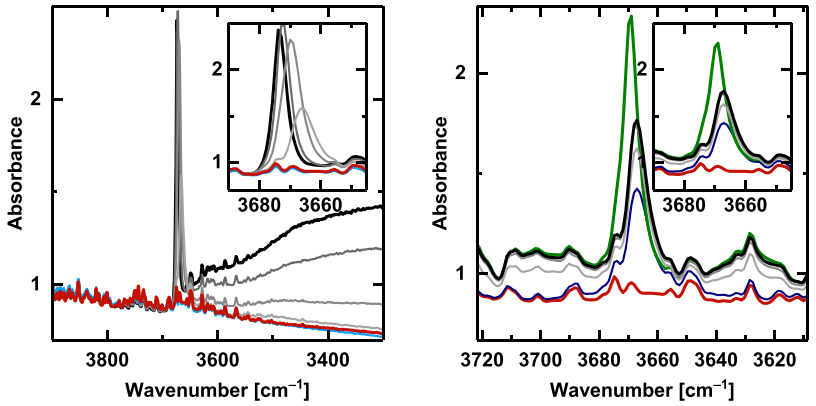

Figure 9. FT−IR spectra of UiO-67-Pt, focusing on Zr-μ_3−OH. Left: During activation. The black spectrum is collected at room temperature, the gray spectra from darkest to brightest are acquired in 10 min intervals during the temperature ramp to 350 °C (5 °C min^{-1}), and the light blue spectrum is acquired when 350 °C is reached. The red curve is obtained after 4 h at 350 °C. Right: Red: as in the left figure. Blue: at 245 °C in 10% H_2, light gray/dark gray/black: 2/3.5/90 min after introducing the reaction feed at 245 °C (CO_2/H_2 = 1/6 mL min^{-1}, 1 bar). Green: after 90 min at 170 °C in reaction feed.

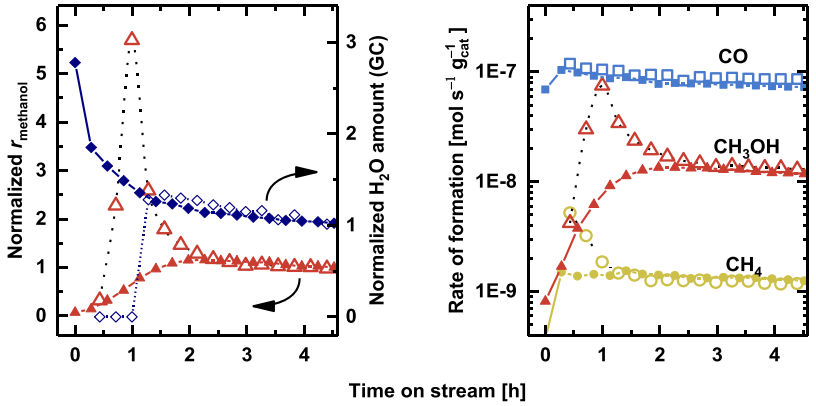

Figure 10. Reaction-onset comparison of the dehydrated (open symbols) and prehydrated UiO-67-Pt (small filled). Left: Normalized methanol formation rate (left axis) and steady state normalized H_2O GC amount (diamonds, right axis) versus time on stream. Right: CO (squares), CH_3OH (triangles), and CH_4 (circles) rate of formation. Reaction conditions: CO_2/H_2/inert = 1/3/1, τ = 0.01 g_{cat} min mL^{-1}, T = 170 °C, 8 bar. Prehydration: 0.023 H_2O/Ar, τ = 0.01 g_{cat} min mL^{-1}, T = 170 °C, 1 bar.

Upon activating the catalyst for CO_2 hydrogenation (i.e., reduction at 350 °C in 10% H_2 for 4 h), the Zr-μ_3−OH groups of the UiO-67 nodes are completely removed via dehydration.[45,46] Figure 9 shows an FT−IR spectrum of the Zr-μ_3−OH region of the sample during activation. The full FT−IR spectrum and its features are described in detail elsewhere.[17,45,47,48] The intense peak of Zr-μ_3−OH at 3669 cm^{-1} decreases with increased temperature, and even before 350 °C is reached, the signal is completely absent. Notably, the dehydration causes a reordering of the Zr-node from Zr_6O_8 (i.e., $Zr_6O_4(OH)_4$), where Zr is 8-coordinated, to a distorted Zr_6O_6 analog where Zr is 7-coordinated.[45,46] The reordering is reversible and does not induce overall changes to the framework structure, nor to the connecting carboxylates.[45] When the temperature is decreased to 245 °C, and a reaction feed of 1/6 CO_2/H_2 is introduced to the IR-cell, the signal of Zr-μ_3−OH increases as H_2O is produced in the reaction, and reaches a plateau in less than 5 min (Figure 9). At 170 °C, under steady state reaction conditions, the signal of Zr-μ_3−OH is larger, compared to 245 °C. Under these conditions, the Zr-μ_3−OH groups are dynamic and H readily exchanges for D during H/D exchange experiments, either by direct H-spillover or via reaction products.[17]

Considering the reaction-onset experiment at 8 bar, we notice that no signal of H_2O was detected in the GC until ∼1 h on stream. Furthermore, the appearance of gas phase H_2O coincided with a substantial drop in the methanol formation rate (Figure 10, left). Interestingly, the molar amount of H_2O formed until it appeared in the GC (calculated from reaction stoichiometry), corresponds to about 40% of the estimated number of Zr-μ_3−OH groups in the MOF. This observation indicates a correlation between the transient regime with higher methanol formation rate and the Zr-nodes' state of hydration and/or the presence of H_2O.

To further investigate the influence of the state of hydration of the Zr-nodes, a reaction-onset experiment was performed starting from a prehydrated catalyst. After the activation procedure, the MOF was exposed to a flow of wet Ar (saturated with H_2O vapor at room temperature) at 170 °C prior to the switch to reaction feed and subsequent pressure increase. The product formation rates with time on stream over the initially dehydrated and prehydrated catalysts are shown in Figure 10 (right). The transient regime is very different in the two measurements. Over the prehydrated catalyst, the methanol peak is gone, and the methanol formation rate instead gradually increases toward steady state, reaching the same value as over the initially dehydrated sample. For methane, the rate of formation starts, and is maintained at the steady state value, which is the same for the dehydrated and prehydrated catalyst.

https://dx.doi.org/10.1021/jacs.0c07153
J. Am. Chem. Soc. 2020, 142, 17105−17118

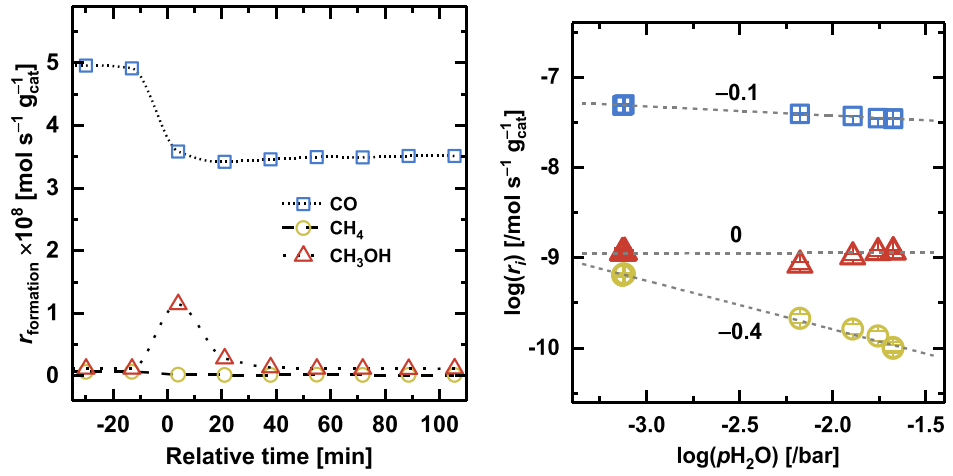

Figure 11. Left: Rate of CO (squares), CH_4 (circles), and CH_3OH (triangles) formation during a switch from $CO_2 + H_2$ to $CO_2 + H_2 + xH_2O$ (x = 1.7 vol %) at time = 0. Right: Influence of pH_2O on the steady state formation rates of CO, methanol and methane. pH_2O is estimated as the sum of the cofed pH_2O and half of the pH_2O produced in the reaction at steady state (calculated from reaction stoichiometry). The in-plot numbers are the respective reaction orders. Units in the right-hand plot represent the variable X in "log(X)". Conditions: CO_2/H_2/inert = 1/6/3 with 0 (yielding an average 0.08), 0.6, 1.2, 1.7, or 2 vol % H_2O, τ = 0.01 g_{cat} min mL^{-1}, T = 170 °C, 1 bar.

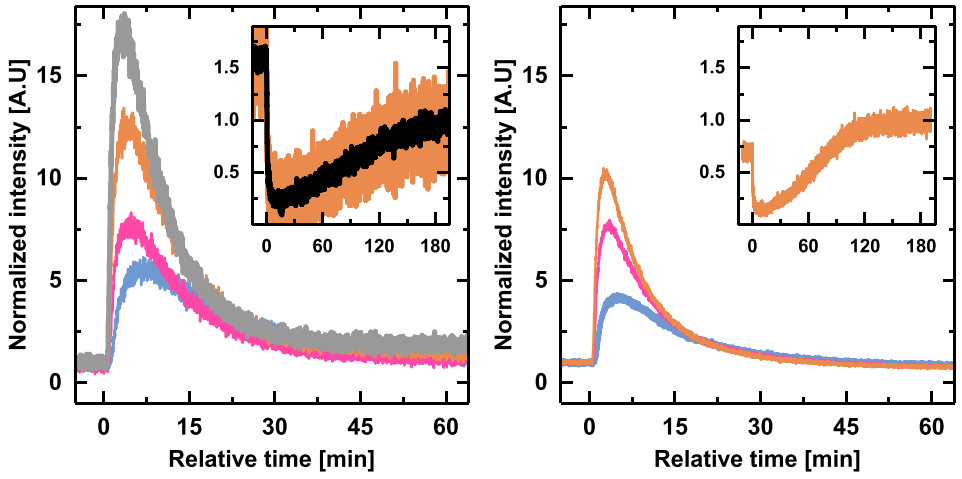

Figure 12. Transient evolution of the normalized methanol formation rate when switching from dry to wet reaction feed, in $CO_2 + H_2$ (left) and $CO_2 + D_2$ (right). H_2O vol % in feed = 0.6 (blue), 1.2 (pink), 1.7 (orange), and 2 (gray). The inset shows the rate of methanol formation when switching from wet (1.7% H_2O) to dry feed. The black trace is a moving average. Conditions: 1/6/3 $CO_2/H_2(D_2)$/Ar ambient pressure, T = 170 °C, τ = 0.01 g_{cat} min mL^{-1}.

This observation adds further evidence to the importance of Zr-node defects in CH_4 formation. No evident change in CO formation is observed. The prehydration results clearly demonstrate that hydration of the Zr-node is of importance, however, this experiment alone cannot distinguish whether it is due to an intrinsic activity difference between the dehydrated and hydrated Zr-node, or due to competitive adsorption between methanol (and methane) and H_2O. The influence of H_2O on the reaction is addressed further in the following section.

Influence of H_2O on the Reaction with Hydrated Nodes. The influence of H_2O on the reaction was investigated through cofeed experiments at 170 °C and ambient pressure (CO_2/H_2/inert = 1/6/3, τ = 0.01 g_{cat} min mL^{-1}). To enable monitoring of transient as well as steady state effects, the reaction feed was switched between feeds of $CO_2 + H_2$ and $CO_2 + H_2 + xH_2O$ (x = 0.6, 1.2, 1.7, and 2 vol %). Figure 11 (left) shows the product formation rates when switching from dry to 1.7% H_2O reaction feed. All three carbon-containing products are affected by the presence of H_2O in the reaction feed. The rates of CO and CH_4 formation decrease to a new steady state within the time resolution of the GC measurements (~16 min), while methanol first increases by more than an order of magnitude then decreases and reaches steady state after ~30 min.

The influence of pH_2O on the reaction rates at steady state is shown in Figure 11 (right). An increasing H_2O pressure has a substantial inhibiting effect on the CH_4 formation rate (−0.4 order), and only minor effect on CO formation rate (−0.1 order). In a previous contribution, we reported that all product formation rates decreased with increasing contact time due to an inhibiting effect of CO and/or H_2O.[17] Reaction orders in p(CO + H_2O) of −1.1, −0.7, and −1.0, for CO, CH_4, and CH_3OH formation were observed. Thus, the reaction orders observed here in pH_2O suggest that for CO, self-inhibition mainly causes the negative effect of contact time on the CO formation rate, while both majority products (CO and H_2O) inhibit CH_4 formation, and only CO inhibits CH_3OH formation.

https://dx.doi.org/10.1021/jacs.0c07153
J. Am. Chem. Soc. 2020, 142, 17105−17118

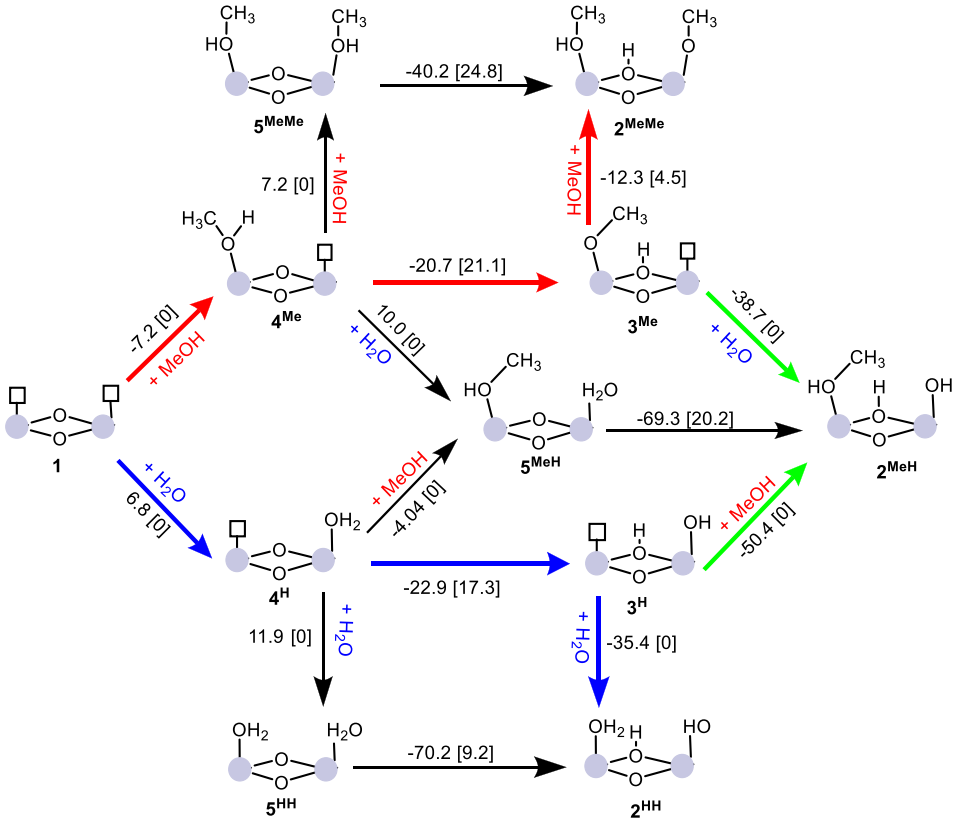

Figure 13. Free energy pathway (T = 170 °C, P = 1 bar) representing the progression of methanol and water adsorption or proton transfers on a defective Zr-node. Reaction-free energies are given between each reaction step. Energy barriers are shown in parentheses. Red arrows represent the preferred pathway for reactions involving only MeOH, blue arrows for reactions involving only water, and green arrows for reactions involving water and methanol. All energies are in kJ/mol.

Although a large transient influence of the introduction of H_2O was observed for methanol formation, the steady state value is unchanged (zero order). However, as seen in Figure 11 (right), the rate of methanol formation at pH_2O = 0.006 ($\log(pH_2O) = -2.2$) is somewhat lower than the rate under "dry conditions" (i.e., no added H_2O, average $\log(pH_2O) = -3.1$), and when the pH_2O increases further, the rate of methanol formation increases slightly (relative to pH_2O = 0.006). When only considering the methanol formation rate under wet conditions in the analysis, the reaction order in pH_2O is estimated to 0.25. If the orders are in fact different at low and high pH_2O, then it may suggest that the reaction proceeds via different pathways or is limited by different elementary steps in the two regimes of pH_2O. To assess the possibility of different reaction pathways/rate-limiting steps further, the influence of H_2O should be investigated at pH_2O values closer to those obtained under the "dry" conditions, as well as in the intermediate range. These pH_2O values are however outside the experimentally achievable range of our test-setup and hence outside the scope of this study.

Having assessed the influence of H_2O at steady state, we turn to the transient influence. Figure 12 (left) shows the intensity of methanol (m/z = 31), normalized to the dry steady state reaction rate, when switching from the dry feed to wet feeds containing different pH_2O. The peak size increases significantly with increasing pH_2O in the wet feed, and integration of the peaks yields an approximate 0.5 order dependence in pH_2O for methanol formed during the transient. Interestingly, when switching back from wet to dry conditions, the methanol formation rate instead decreases rapidly, and then slowly increases to the dry steady state value. The normalized intensity of methanol during the switch from 1.7% to 0% H_2O in the feed is shown in the inset in Figure 12. Changing from wet to dry conditions, the approach to steady state is somewhat slower, as compared to from dry to wet, but the magnitude of the transient change increases with pH_2O in both cases, i.e., the gas phase methanol concentration decreases with increasing pH_2O. The highly similar, but inverse, behavior of methanol during switches from dry versus wet reaction conditions indicates that the two transients are caused by reversible adsorption/desorption phenomena. Prior studies of other materials showed that methanol may adsorb and form a methoxy group. Water may subsequently react with the methoxy group to reform gas-phase methanol.[49−53] Such interactions could explain the transient changes in methanol. However, under identical conditions, no methoxy groups were observed during operando FT−IR of UiO-67-Pt.[17] However, Larmier et al. observed methoxy groups on Cu/ZrO_2 by in situ DRIFTS when exposed to CO_2 and H_2 (1:3) under 5 bar pressure and 230 °C (closed system), and by ex situ solid-state NMR after exposure for 12 h.[10]

To get further insights into the mechanism of transient methanol formation, identical experiments were performed using D_2 instead of H_2, i.e., switching from $CO_2 + D_2$ to $CO_2 + D_2 + xH_2O$. By this approach, it is possible to identify the source of hydrogen in the desorbed methanol. At steady state, the influence of pH_2O on the reaction rates in D_2 (Figure 12, right) is unchanged for CO (−0.1) and slightly less negative for methane (−0.3), as compared to H_2. For methanol a negative 0.2 order in pH_2O is observed, and the slope (SI Figure S11) is linear in the whole pH_2O range, including dry conditions.

https://dx.doi.org/10.1021/jacs.0c07153
J. Am. Chem. Soc. 2020, 142, 17105−17118

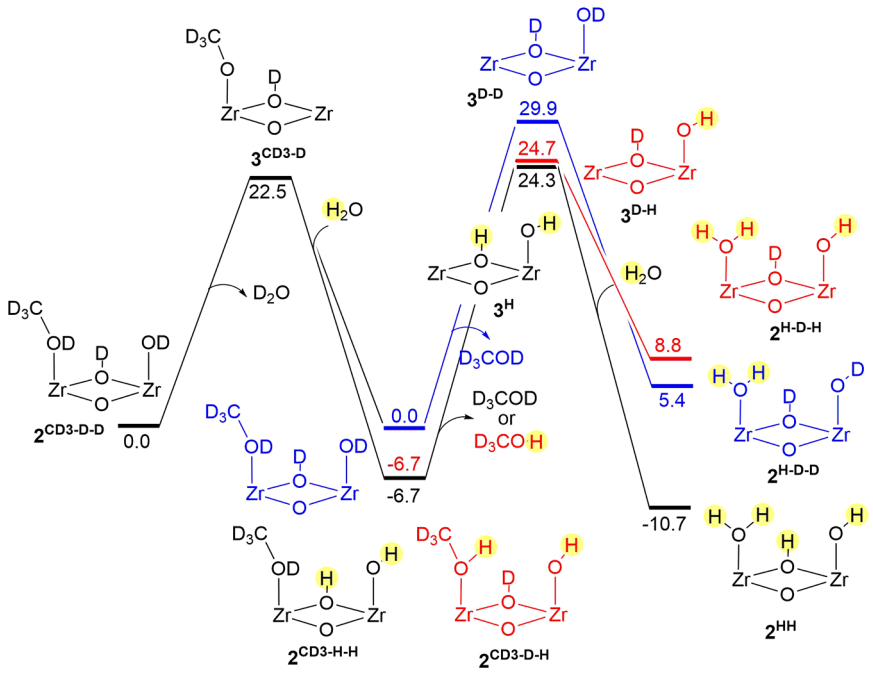

Figure 14. Free energy diagram (T = 170 °C, P = 1 bar) showing the most plausible pathway for the proton transfer to form and desorb methanol in the scheme in Figure S13 with all energies in kJ/mol.

Considering the high complexity of the role of H_2O and its influence on the reaction, the origin of this isotope effect is likely manifold.

Turning next to the transient regime, Figure 12 (right) shows the intensity of methanol (m/z = 34), normalized to the dry steady state reaction rate, when switching from the dry feed to wet feeds of different pH_2O. The same trend is observed in D_2 as in H_2; the peak size of methanol desorption and adsorption increases with pH_2O. Considering the source of hydrogen, interestingly, the desorbed methanol does not contain significant amounts of H from H_2O. This suggests that methanol desorption via protonation of OCD_3 by H_2O is not the main pathway.

The amount of methanol produced during the transient (in D_2) is approximately 18, 25, and 33 μmol g_{cat}^{-1} for pH_2O = 0.006, 0.012, and 0.017, respectively. These amounts are comparable to the number of intermediates (23 μmol g_{cat}^{-1}) leading to methanol formation determined from ^{13}C-SSITKA under identical, dry, conditions (see Figure 8 and Table 3).

To further understand the role of water in methanol desorption, the free energy pathways for the adsorption of water and methanol to a hydrated Zr-node with one missing linker were calculated at 170 °C (Figure 13 and SI Table S3). Starting from the missing linker structure (**1**), which involves two Zr-vacant sites and two μ-O bridges, coordination of water and methanol followed by proton transfer reactions generate the 11 intermediates shown in Figure 13. These intermediates have been labeled by using numbers, to indicate species with different substituents at Zr, and superscript H and/or Me to indicate whether the origin of the substituent is water and/or methanol, respectively. The calculated energy barriers connecting these intermediates are in all cases very low (<25 kJ/mol for proton transfer reactions and 0 kJ/mol for adsorption of methanol and water in Zr-vacant sites). Therefore, the pathway is mainly dictated by thermodynamics. In the presence of MeOH, the formation of the most stable intermediate $\mathbf{2}^{\mathbf{MeMe}}$, where methanol is adsorbed on one of the Zr sites (Zr-CH_3OH), methoxy is adsorbed on the other Zr site (Zr-OCH_3) and a proton is adsorbed on one of the μ-O sites (μ-OH), is exergonic by 40.2 kJ/mol. The analogous process with water has a $\Delta G(\mathbf{1} + H_2O + H_2O \rightarrow \mathbf{2}^{\mathbf{HH}})$ = −51.5 kJ/mol, which is 11.3 kJ/mol lower than with methanol. However, in the presence of both species at equal concentration, intermediate $\mathbf{2}^{\mathbf{MeH}}$, where methanol is adsorbed to one Zr site (Zr−CH_3OH), a hydroxyl is adsorbed to the other Zr site (Zr−OH) and a proton is adsorbed to one of the μ-O sites (μ-OH), is the most stable with a $\Delta G(\mathbf{1} + H_2O + MeOH \rightarrow \mathbf{2}^{\mathbf{MeH}})$ = −66.6 kJ/mol. Attempts to optimize an intermediate involving Zr−OCH_3 and Zr−OH_2 were unsuccessful.[54] $\mathbf{2}^{\mathbf{MeH}}$ is therefore predicted to be the most abundant species at equilibrium, even though all intermediates are accessible at the reaction conditions. The preference for $\mathbf{2}^{\mathbf{MeH}}$ was also confirmed using a microkinetic model (MKM) constructed with all possible pathways shown in Figure 13. The MKM showed that, at equal or larger concentrations of water compared to methanol (as expected for a CO_2 hydrogenation reaction yielding CO as the main product), the concentration of species containing methoxy groups ($\mathbf{3}^{\mathbf{Me}}$ and $\mathbf{5}^{\mathbf{MeMe}}$) were very low (∼0 mol/L), which is consistent with them not being observed under experimental conditions. Using 1 M of **1**, H_2O and MeOH, 0.98 M of $\mathbf{2}^{\mathbf{MeH}}$ is observed; while using 1 M of **1** and water, and 0.03 of MeOH, the species observed are $\mathbf{2}^{\mathbf{MeH}}$ (0.03 M), $\mathbf{2}^{\mathbf{HH}}$ (0.5 M), $\mathbf{3}^{\mathbf{H}}$ (0.034 M), and **1** (0.5 M). The latter result suggests that $\mathbf{3}^{\mathbf{H}}$ is never a main species but $\mathbf{2}^{\mathbf{HH}}$ or **1**, which may be relevant in alcohol dehydration processes.[38,55]

As discussed above (Figure 12), cofeed experiments shows that adding water into the system increases the observed methanol concentration initially. To gain further insight into this experimental observation, we set up a MKM where the equilibrated structure $\mathbf{2}^{\mathbf{MeH}}$ at 1 mol/L concentration was used as a starting point and then different amounts of water is introduced to the system (see SI Figure S12). These simulations show that when any additional water was introduced into the

https://dx.doi.org/10.1021/jacs.0c07153
J. Am. Chem. Soc. 2020, 142, 17105−17118

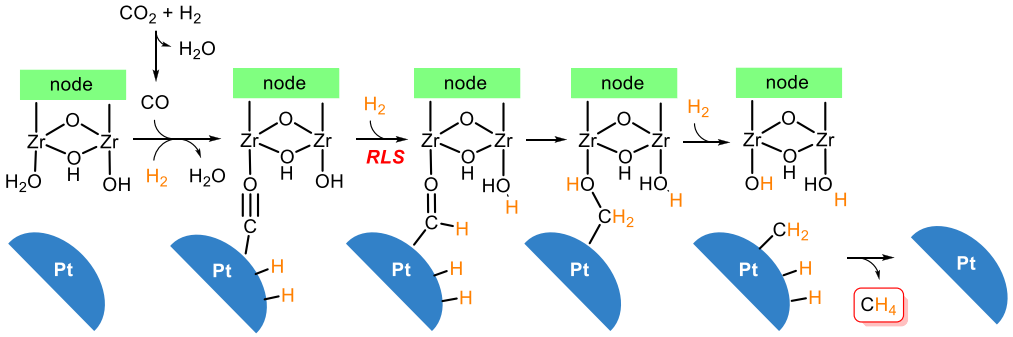

Figure 15. Postulated mechanism for methane formation on an open Zr-site at the UiO-67-Pt Zr-node.

system it causes methanol to desorb from the system, in agreement with the experimental observations. The adsorbed methanol is desorbed from the Zr-site and is replaced by a water molecule, resulting in structure $\mathbf{2}^{\mathbf{HH}}$ in Figure 13. The equilibria $\mathbf{2}^{\mathbf{MeH}} \leftrightarrow \mathbf{3}^{\mathbf{H}} \leftrightarrow \mathbf{2}^{\mathbf{HH}}$ is in agreement with the nonobservation of CD_3OH in the experiments performed with CO_2 and D_2 followed by addition of H_2O (see Figure 7, in which the orange H could be D). However, the equilibria between $\mathbf{2}^{\mathbf{MeH}}$ and $\mathbf{3}^{\mathbf{Me}}$, which is thermodynamically preferred, could also play a role in the reaction leading to H/D-exchange. To determine the relevance of this process, DFT calculations were performed considering deuterated species and different proton-transfer mechanisms (Figures 14 and S13). All mechanisms proceed without any additional energy barriers beyond thermodynamics. Figure 14 shows that the relative energy of $\mathbf{3}^{\mathbf{H}}$ compared to $\mathbf{2}^{\mathbf{CD3\text{-}D\text{-}D}}$ (ΔG = 24.3 kJ/mol) decreases significantly compared to the analogous intermediates without −D ($\mathbf{3}^{\mathbf{H}}$ and $\mathbf{2}^{\mathbf{MeH}}$, ΔG = 50.4 kJ/mol, in Figure 13). In addition, intermediate $\mathbf{2}^{\mathbf{H-H}}$ becomes the most preferred intermediate compared to $\mathbf{2}^{\mathbf{CD3\text{-}D\text{-}D}}$, $\mathbf{2}^{\mathbf{CD3\text{-}H\text{-}D}}$, or $\mathbf{2}^{\mathbf{CD3-H-H}}$, favoring the desorption of CD_3OD (see Table S4). Nevertheless, these energy differences are created because of the isotope exchange, and will not exist in a normal experiment using H_2, in which the proton in desorbed methanol may originate from either water already present or newly added.

An interesting result from the energies shown in Figure 13 is that the adsorption of methanol in **1** (ΔG = −7.2 kJ/mol) is less favorable than in $\mathbf{3}^{\mathbf{H}}$ (ΔG = −50.4 kJ/mol) by 43.2 kJ/mol. Clearly, methanol is more strongly adsorbed to a hydrated node than to a dehydrated node, which could partially account for the larger methanol formation rate at the reaction-onset (due to more rapid liberation of the defective Zr site for another reaction cycle) (see Figure 10). A similar result has already been reported for water in defective UiO-66 type MOFs.[56,57] Structural and electronic analysis of **1**, $\mathbf{4}^{\mathbf{Me}}$, $\mathbf{3}^{\mathbf{H}}$, and $\mathbf{2}^{\mathbf{MeH}}$ suggest that the reason for the larger adsorption energies for MeOH in $\mathbf{3}^{\mathbf{H}}$ is the formation of an H-bond between MeOH and the terminal OH (see SI). We also wanted to evaluate the influence of having two missing linkers in the methanol and water adsorption (see Table S5). With this goal, we built two model systems, in which two missing linkers in adjacent ($\mathbf{3}^{\mathbf{H}}$**-adj**) and opposite ($\mathbf{3}^{\mathbf{H}}$**-opp**) positions were replaced by −OH groups (see Figure 1), and calculated the methanol adsorption in each model. The free energy for the first and second methanol adsorption with $\mathbf{3}^{\mathbf{H}}$**-adj** are 3.2 and 66.9 kJ/mol; while with $\mathbf{3}^{\mathbf{H}}$**-opp**, they are −39.3 and −35.6 kJ/mol, respectively. These energies show that methanol binds stronger on a node with a single missing linker ($\mathbf{3}^{\mathbf{H}}$, ΔG = −50.4 kJ/mol) than on nodes with an additional, adjacent, or opposite, missing linker defect. In the case of adjacent linkers, the adsorption energies change drastically, especially in the case where water is coordinated to one Zr-atom attached to an OH group (ΔG = +66.9 kJ/mol). This result strongly suggests that having a larger number of defects not only increases the number of active sites to produce methanol but also facilitates methanol desorption.

These results show that both water and missing linkers play an important role in methanol desorption by either displacing the equilibria or changing the methanol adsorption energies. However, Figure 10 suggests that water does not have an important influence on the MeOH formation rate at steady state. Instead, it decreases the rate of methane significantly. An explanation to this observation is the following: As represented in Figure 15, interaction of adsorbed CO with a Zr atom from a node should be feasible at the interface between Pt NPs and Zr nodes. This coordination would increase the electophilicity of C and favor the hydride transfer, which has been proposed to be the rate-limiting step for the CO hydrogenation to methane with Pt-NPs.[58] When adding water to the system, the equilibria between CO and water will be displaced favoring water coordination and disfavoring methane formation. In the case of methanol (see Figure 7), this competition takes place before the formation of formate, which is thermodynamically preferred of having $\mathbf{2}^{\mathbf{HH}}$. Therefore, it would not influence the rate-limiting step of methanol, which has been proposed to be the hydrogenation of formate.

CONCLUSIONS

The dynamic role of the Zr-node during CO_2 hydrogenation over UiO-67-Pt and the influence of defects and water on the reaction have been investigated by steady state and isotope transient kinetic studies, as well as water cofeed experiments.

A UiO-67-Pt MOF catalyst was designed with fewer defects to influence the rate of methanol formation. ^{13}C-SSITKA experiments verified that a lower number of defect sites led to lower methanol formation rates, and that this decrease was caused by a lower number of surface intermediates. This result serves as a proof-of-principle in rational design of a MOF catalyst based on fundamental understanding. Importantly, the methane formation rate had a similar dependency of Zr node defects, while the CO formation rate was almost invariant with defect density. These results strongly suggest that the rate-limiting step of CO formation occurs at the Pt NPs, while the rate-limiting step of methane formation, like methanol, takes place at the Pt NP−Zr node interface.

By comparing the onset of reaction over a sample with dehydrated Zr-nodes to the onset over a prehydrated sample, it was found that the rate of methanol and methane formation are both higher over a dehydrated node than over a hydrated node. Adding surplus water to the feed has an inhibiting effect on

https://dx.doi.org/10.1021/jacs.0c07153
J. Am. Chem. Soc. 2020, 142, 17105−17118

methane formation, but not on methanol formation, suggesting that methanol selectivity may be optimized by steam addition to the reactant gas feed. Moreover, transient H_2O cofeed experiments showed that the introduction of H_2O causes substantial amounts of methanol to desorb from the catalyst; while removal of H_2O causes readsorption. No transfer of hydrogen from H_2O to the desorbed methanol was observed, suggesting that the cause of desorption is competitive adsorption. DFT calculations showed that methanol is adsorbed more weakly on less hydrated and more defective nodes, which can contribute to the observation of larger amounts of methanol with these systems.

■ ASSOCIATED CONTENT

Supporting Information

The Supporting Information is available free of charge at https://pubs.acs.org/doi/10.1021/jacs.0c07153.

XRD, N_2 adsorption isotherms, solution state NMR, STEM, additional catalytic test data, XPS, CO_2 adsorption isotherms, computational details, and additional computational data (PDF)

Geometries for all computed structures (XYZ)

■ AUTHOR INFORMATION

Corresponding Authors

Unni Olsbye − *Centre for Materials Science and Nanotechnology, Department of Chemistry, University of Oslo, N-0315 Oslo, Norway;* orcid.org/0000-0003-3693-2857; Email: unni.olsbye@kjemi.uio.no

Ainara Nova − *Hylleraas Centre for Quantum Molecular Sciences, Department of Chemistry, University of Oslo, N-0315 Oslo, Norway;* orcid.org/0000-0003-3368-7702; Email: ainara.nova@kjemi.uio.no

Authors

Emil Sebastian Gutterød − *Centre for Materials Science and Nanotechnology, Department of Chemistry, University of Oslo, N-0315 Oslo, Norway*

Sri Harsha Pulumati − *Science Institute and Faculty of Industrial Engineering, Mechanical Engineering and Computer Science, University of Iceland, 107, Iceland*

Gurpreet Kaur − *Centre for Materials Science and Nanotechnology, Department of Chemistry, University of Oslo, N-0315 Oslo, Norway*

Andrea Lazzarini − *Centre for Materials Science and Nanotechnology, Department of Chemistry, University of Oslo, N-0315 Oslo, Norway;* orcid.org/0000-0002-0404-6597

Bjørn Gading Solemsli − *Centre for Materials Science and Nanotechnology, Department of Chemistry, University of Oslo, N-0315 Oslo, Norway*

Anette Eleonora Gunnæs − *Centre for Materials Science and Nanotechnology, Department of Physics, University of Oslo, N-0349 Oslo, Norway*

Christian Ahoba-Sam − *Centre for Materials Science and Nanotechnology, Department of Chemistry, University of Oslo, N-0315 Oslo, Norway*

Maria Evangelou Kalyva − *Centre for Materials Science and Nanotechnology, Department of Chemistry, University of Oslo, N-0315 Oslo, Norway*

Johnny Andreas Sannes − *Centre for Materials Science and Nanotechnology, Department of Chemistry, University of Oslo, N-0315 Oslo, Norway*

Stian Svelle − *Centre for Materials Science and Nanotechnology, Department of Chemistry, University of Oslo, N-0315 Oslo, Norway;* orcid.org/0000-0002-7468-5546

Egill Skúlason − *Science Institute and Faculty of Industrial Engineering, Mechanical Engineering and Computer Science, University of Iceland, 107, Iceland;* orcid.org/0000-0002-0724-680X

Complete contact information is available at: https://pubs.acs.org/10.1021/jacs.0c07153

Notes

The authors declare no competing financial interest.

■ ACKNOWLEDGMENTS

E.S.G, G.K., A.L., S.S., and U.O. acknowledge the Research Council of Norway for financial support (FRINATEK TopPForsk Grant No. 250795 CONFINE). H.P., E.S., and A.N. acknowledge support by the "Nordic Consortium for CO_2 Conversion" (NordForsk project No. 85378, site.uit.no/nordco2) and the Norwegian Metacenter for Computational Science (NOTUR) for computational resources (project number nn4654k). A.N. acknowledge the support from the Research Council of Norway (FRINATEK Grant No. 250044 and Center of Excellence Grant No. 262695). B.G.S. and A.E.G. acknowledge the Research Council of Norway for its support of the Norwegian Center for Transmission Electron Microscopy (NORTEM) (197405/F50).

■ REFERENCES

(1) Aresta, M.; Dibenedetto, A.; Angelini, A. The changing paradigm in CO2 utilization. *J. CO2 Util.* **2013**, *3*−*4*, 65−73.

(2) Olah, G. A. Beyond Oil and Gas: The Methanol Economy. *Angew. Chem., Int. Ed.* **2005**, *44* (18), 2636−2639.

(3) Matzen, M.; Demirel, Y. Methanol and dimethyl ether from renewable hydrogen and carbon dioxide: Alternative fuels production and life-cycle assessment. *J. Cleaner Prod.* **2016**, *139*, 1068−1077.

(4) Kattel, S.; Liu, P.; Chen, J. G. Tuning Selectivity of CO2 Hydrogenation Reactions at the Metal/Oxide Interface. *J. Am. Chem. Soc.* **2017**, *139* (29), 9739−9754.

(5) Li, K.; Chen, J. G. CO2 Hydrogenation to Methanol over ZrO2-Containing Catalysts: Insights into ZrO2 Induced Synergy. *ACS Catal.* **2019**, *9* (9), 7840−7861.

(6) Meunier, F. C. Mixing Copper Nanoparticles and ZnO Nanocrystals: A Route towards Understanding the Hydrogenation of CO2 to Methanol? *Angew. Chem., Int. Ed.* **2011**, *50* (18), 4053−4054.

(7) Rodriguez, J. A.; Liu, P.; Stacchiola, D. J.; Senanayake, S. D.; White, M. G.; Chen, J. G. Hydrogenation of CO2 to Methanol: Importance of Metal−Oxide and Metal−Carbide Interfaces in the Activation of CO2. *ACS Catal.* **2015**, *5* (11), 6696−6706.

(8) Roy, S.; Cherevotan, A.; Peter, S. C. Thermochemical CO2 Hydrogenation to Single Carbon Products: Scientific and Technological Challenges. *ACS Energy Lett.* **2018**, *3* (8), 1938−1966.

(9) Lam, E.; Larmier, K.; Wolf, P.; Tada, S.; Safonova, O. V.; Copéret, C. Isolated Zr Surface Sites on Silica Promote Hydrogenation of CO2 to CH3OH in Supported Cu Catalysts. *J. Am. Chem. Soc.* **2018**, *140* (33), 10530−10535.

(10) Larmier, K.; Liao, W.-C.; Tada, S.; Lam, E.; Verel, R.; Bansode, A.; Urakawa, A.; Comas-Vives, A.; Copéret, C. CO2-to-Methanol Hydrogenation on Zirconia-Supported Copper Nanoparticles: Reaction Intermediates and the Role of the Metal−Support Interface. *Angew. Chem., Int. Ed.* **2017**, *56* (9), 2318−2323.

(11) Lam, E.; Larmier, K.; Tada, S.; Wolf, P.; Safonova, O. V.; Copéret, C. Zr(IV) surface sites determine CH3OH formation rate on Cu/ZrO2/SiO2- CO2 hydrogenation catalysts. *Chin. J. Catal.* **2019**, *40* (11), 1741−1748.

(12) Lam, E.; Corral-Pérez, J. J.; Larmier, K.; Noh, G.; Wolf, P.; Comas-Vives, A.; Urakawa, A.; Copéret, C. CO2 Hydrogenation on Cu/Al2O3: Role of the Metal/Support Interface in Driving Activity and Selectivity of a Bifunctional Catalyst. *Angew. Chem.* **2019**, *131* (39), 14127−14134.
(13) Ferri, D.; Burgi, T.; Baiker, A. Probing boundary sites on a Pt/Al2O3 model catalyst by CO2 hydrogenation and in situ ATR-IR spectroscopy of catalytic solid-liquid interfaces. *Phys. Chem. Chem. Phys.* **2002**, *4* (12), 2667−2672.
(14) Rungtaweevoranit, B.; Baek, J.; Araujo, J. R.; Archanjo, B. S.; Choi, K. M.; Yaghi, O. M.; Somorjai, G. A. Copper Nanocrystals Encapsulated in Zr-based Metal−Organic Frameworks for Highly Selective CO2 Hydrogenation to Methanol. *Nano Lett.* **2016**, *16* (12), 7645−7649.
(15) An, B.; Zhang, J.; Cheng, K.; Ji, P.; Wang, C.; Lin, W. Confinement of Ultrasmall Cu/ZnOx Nanoparticles in Metal−Organic Frameworks for Selective Methanol Synthesis from Catalytic Hydrogenation of CO2. *J. Am. Chem. Soc.* **2017**, *139* (10), 3834−3840.
(16) Gutterød, E. S.; Øien-Ødegaard, S.; Bossers, K.; Nieuwelink, A.-E.; Manzoli, M.; Braglia, L.; Lazzarini, A.; Borfecchia, E.; Ahmadigoltapeh, S.; Bouchevreau, B.; Lønstad-Bleken, B. T.; Henry, R.; Lamberti, C.; Bordiga, S.; Weckhuysen, B. M.; Lillerud, K. P.; Olsbye, U. CO2 Hydrogenation over Pt-Containing UiO-67 Zr-MOFs—The Base Case. *Ind. Eng. Chem. Res.* **2017**, *56* (45), 13206−13218.
(17) Gutterød, E. S.; Lazzarini, A.; Fjermestad, T.; Kaur, G.; Manzoli, M.; Bordiga, S.; Svelle, S.; Lillerud, K. P.; Skulason, E.; Øien-Ødegaard, S.; Nova, A.; Olsbye, U. Hydrogenation of CO2 to Methanol by Pt Nanoparticles Encapsulated in UiO-67: Deciphering the Role of the MOF. *J. Am. Chem. Soc.* **2020**, *142* (2), 999−1009.
(18) Li, X.; Liu, G.; Xu, D.; Hong, X.; Edman Tsang, S. C. Confinement of subnanometric PdZn at a defect enriched ZnO/ZIF-8 interface for efficient and selective CO2 hydrogenation to methanol. *J. Mater. Chem. A* **2019**, *7* (41), 23878−23885.
(19) Gutov, O. V.; Hevia, M. G.; Escudero-Adán, E. C.; Shafir, A. Metal−Organic Framework (MOF) Defects under Control: Insights into the Missing Linker Sites and Their Implication in the Reactivity of Zirconium-Based Frameworks. *Inorg. Chem.* **2015**, *54* (17), 8396−8400.
(20) Braglia, L.; Borfecchia, E.; Lomachenko, K. A.; Bugaev, A. L.; Guda, A. A.; Soldatov, A. V.; Bleken, B. T. L.; Øien-Ødegaard, S.; Olsbye, U.; Lillerud, K. P.; Bordiga, S.; Agostini, G.; Manzoli, M.; Lamberti, C. Tuning Pt and Cu sites population inside functionalized UiO-67 MOF by controlling activation conditions. *Faraday Discuss.* **2017**, *201* (0), 265−286.
(21) Øien, S.; Agostini, G.; Svelle, S.; Borfecchia, E.; Lomachenko, K. A.; Mino, L.; Gallo, E.; Bordiga, S.; Olsbye, U.; Lillerud, K. P.; Lamberti, C. Probing Reactive Platinum Sites in UiO-67 Zirconium Metal−Organic Frameworks. *Chem. Mater.* **2015**, *27* (3), 1042−1056.
(22) Inoue, T.; Iizuka, T. Hydrogenation of carbon dioxide and carbon monoxide over supported platinum catalysts. *J. Chem. Soc., Faraday Trans. 1* **1986**, *82* (6), 1681−1686.
(23) VandeVondele, J.; Krack, M.; Mohamed, F.; Parrinello, M.; Chassaing, T.; Hutter, J. Quickstep: Fast and accurate density functional calculations using a mixed Gaussian and plane waves approach. *Comput. Phys. Commun.* **2005**, *167* (2), 103−128.
(24) LIPPERT, G.; HUTTER, J.; PARRINELLO, M. Michele, A hybrid Gaussian and plane wave density functional scheme. *Mol. Phys.* **1997**, *92* (3), 477−487.
(25) Lippert, G.; Hutter, J.; Parrinello, M. The Gaussian and augmented-plane-wave density functional method for ab initio molecular dynamics simulations. *Theor. Chem. Acc.* **1999**, *103* (2), 124−140.
(26) Genovese, L.; Deutsch, T.; Neelov, A.; Goedecker, S.; Beylkin, G. Efficient solution of Poisson's equation with free boundary conditions. *J. Chem. Phys.* **2006**, *125* (7), 074105.
(27) Marek, A.; Blum, V.; Johanni, R.; Havu, V.; Lang, B.; Auckenthaler, T.; Heinecke, A.; Bungartz, H.-J.; Lederer, H. The ELPA library: scalable parallel eigenvalue solutions for electronic structure theory and computational science. *J. Phys.: Condens. Matter* **2014**, *26* (21), 213201.
(28) Perdew, J. P.; Burke, K.; Ernzerhof, M. Generalized Gradient Approximation Made Simple. *Phys. Rev. Lett.* **1996**, *77* (18), 3865−3868.
(29) Grimme, S.; Ehrlich, S.; Goerigk, L. Effect of the damping function in dispersion corrected density functional theory. *J. Comput. Chem.* **2011**, *32* (7), 1456−1465.
(30) Goedecker, S.; Teter, M.; Hutter, J. Separable dual-space Gaussian pseudopotentials. *Phys. Rev. B: Condens. Matter Mater. Phys.* **1996**, *54* (3), 1703−1710.
(31) Krack, M. Pseudopotentials for H to Kr optimized for gradient-corrected exchange-correlation functionals. *Theor. Chem. Acc.* **2005**, *114* (1), 145−152.
(32) Henkelman, G.; Jónsson, H. Improved tangent estimate in the nudged elastic band method for finding minimum energy paths and saddle points. *J. Chem. Phys.* **2000**, *113* (22), 9978−9985.
(33) Henkelman, G.; Uberuaga, B. P.; Jónsson, H. A climbing image nudged elastic band method for finding saddle points and minimum energy paths. *J. Chem. Phys.* **2000**, *113* (22), 9901−9904.
(34) Hoops, S.; Sahle, S.; Gauges, R.; Lee, C.; Pahle, J.; Simus, N.; Singhal, M.; Xu, L.; Mendes, P.; Kummer, U. COPASI—a COmplex PAthway SImulator. *Bioinformatics* **2006**, *22* (24), 3067−3074.
(35) Øien, S.; Wragg, D.; Reinsch, H.; Svelle, S.; Bordiga, S.; Lamberti, C.; Lillerud, K. P. Detailed structure analysis of atomic positions and defects in zirconium metal−organic frameworks. *Cryst. Growth Des.* **2014**, *14* (11), 5370−5372.
(36) Trickett, C. A.; Gagnon, K. J.; Lee, S.; Gándara, F.; Bürgi, H. B.; Yaghi, O. M. Definitive molecular level characterization of defects in UiO-66 crystals. *Angew. Chem., Int. Ed.* **2015**, *54* (38), 11162−11167.
(37) Shearer, G. C.; Chavan, S.; Ethiraj, J.; Vitillo, J. G.; Svelle, S.; Olsbye, U.; Lamberti, C.; Bordiga, S.; Lillerud, K. P. Tuned to perfection: ironing out the defects in metal−organic framework UiO-66. *Chem. Mater.* **2014**, *26* (14), 4068−4071.
(38) Yang, D.; Ortuño, M. A.; Bernales, V.; Cramer, C. J.; Gagliardi, L.; Gates, B. C. Structure and dynamics of Zr6O8 metal−organic framework node surfaces probed with ethanol dehydration as a catalytic test reaction. *J. Am. Chem. Soc.* **2018**, *140* (10), 3751−3759.
(39) Shearer, G. C.; Chavan, S.; Bordiga, S.; Svelle, S.; Olsbye, U.; Lillerud, K. P. Defect Engineering: Tuning the Porosity and Composition of the Metal−Organic Framework UiO-66 via Modulated Synthesis. *Chem. Mater.* **2016**, *28* (11), 3749−3761.
(40) Kaur, G.; Øien-Ødegaard, S.; Lazzarini, A.; Chavan, S. M.; Bordiga, S.; Lillerud, K. P.; Olsbye, U. Controlling the Synthesis of Metal−Organic Framework UiO-67 by Tuning Its Kinetic Driving Force. *Cryst. Growth Des.* **2019**, *19* (8), 4246−4251.
(41) Øien-Ødegaard, S.; Bouchevreau, B.; Hylland, K.; Wu, L.; Blom, R.; Grande, C.; Olsbye, U.; Tilset, M.; Lillerud, K. P. UiO-67-type Metal−Organic Frameworks with Enhanced Water Stability and Methane Adsorption Capacity. *Inorg. Chem.* **2016**, *55* (5), 1986−1991.
(42) Kunkes, E. L.; Studt, F.; Abild-Pedersen, F.; Schlögl, R.; Behrens, M. Hydrogenation of CO2 to methanol and CO on Cu/ZnO/Al2O3: Is there a common intermediate or not? *J. Catal.* **2015**, *328*, 43−48.
(43) Ledesma, C.; Yang, J.; Chen, D.; Holmen, A. Recent Approaches in Mechanistic and Kinetic Studies of Catalytic Reactions Using SSITKA Technique. *ACS Catal.* **2014**, *4* (12), 4527−4547.
(44) Shannon, S. L.; Goodwin, J. G. Characterization of Catalytic Surfaces by Isotopic-Transient Kinetics during Steady-State Reaction. *Chem. Rev.* **1995**, *95* (3), 677−695.
(45) Cavka, J. H.; Jakobsen, S.; Olsbye, U.; Guillou, N.; Lamberti, C.; Bordiga, S.; Lillerud, K. P. A New Zirconium Inorganic Building Brick Forming Metal Organic Frameworks with Exceptional Stability. *J. Am. Chem. Soc.* **2008**, *130* (42), 13850−13851.
(46) Valenzano, L.; Civalleri, B.; Chavan, S.; Bordiga, S.; Nilsen, M. H.; Jakobsen, S.; Lillerud, K. P.; Lamberti, C. Disclosing the Complex Structure of UiO-66 Metal Organic Framework: A Synergic Combination of Experiment and Theory. *Chem. Mater.* **2011**, *23* (7), 1700−1718.

https://dx.doi.org/10.1021/jacs.0c07153
J. Am. Chem. Soc. 2020, 142, 17105−17118

(47) Chavan, S.; Vitillo, J. G.; Gianolio, D.; Zavorotynska, O.; Civalleri, B.; Jakobsen, S.; Nilsen, M. H.; Valenzano, L.; Lamberti, C.; Lillerud, K. P.; Bordiga, S. H2storage in isostructural UiO-67 and UiO-66 MOFs. *Phys. Chem. Chem. Phys.* **2012**, *14* (5), 1614−1626.
(48) Shearer, G. C.; Forselv, S.; Chavan, S.; Bordiga, S.; Mathisen, K.; Bjørgen, M.; Svelle, S.; Lillerud, K. P. In Situ Infrared Spectroscopic and Gravimetric Characterisation of the Solvent Removal and Dehydroxylation of the Metal Organic Frameworks UiO-66 and UiO-67. *Top. Catal.* **2013**, *56* (9), 770−782.
(49) Dyballa, M.; Thorshaug, K.; Pappas, D. K.; Borfecchia, E.; Kvande, K.; Bordiga, S.; Berlier, G.; Lazzarini, A.; Olsbye, U.; Beato, P.; Svelle, S.; Arstad, B. Zeolite Surface Methoxy Groups as Key Intermediates in the Stepwise Conversion of Methane to Methanol. *ChemCatChem* **2019**, *11* (20), 5022−5026.
(50) Edwards, J. F.; Schrader, G. L. Methanol, formaldehyde, and formic acid adsorption on methanol synthesis catalysts. *J. Phys. Chem.* **1985**, *89* (5), 782−788.
(51) Pelmenschikov, A. G.; Morosi, G.; Gamba, A.; Zecchina, A.; Bordiga, S.; Paukshtis, E. A. Mechanisms of methanol adsorption on silicalite and silica: IR spectra and ab-initio calculations. *J. Phys. Chem.* **1993**, *97* (46), 11979−11986.
(52) Wang, Z.; Xiong, F.; Sun, G.; Jin, Y.; Huang, W. Structural Dependence of Competitive Adsorption of Water and Methanol on TiO2 Surfaces. *Chin. J. Chem.* **2017**, *35* (6), 889−895.
(53) Alayon, E. M.; Nachtegaal, M.; Ranocchiari, M.; van Bokhoven, J. A. Catalytic conversion of methane to methanol over Cu-mordenite. *Chem. Commun.* **2012**, *48* (3), 404−406.
(54) A proton transfer from the adsorbed OH_2 to OCH_3 is observed during geometry optimization.
(55) Yang, D.; Gaggioli, C. A.; Ray, D.; Babucci, M.; Gagliardi, L.; Gates, B. C. Tuning Catalytic Sites on Zr6O8Metal−Organic Framework Nodes via Ligand and Defect Chemistry Probed with tert-Butyl Alcohol Dehydration to Isobutylene. *J. Am. Chem. Soc.* **2020**, *142* (17), 8044−8056.
(56) Vandichel, M.; Hajek, J.; Ghysels, A.; De Vos, A.; Waroquier, M.; Van Speybroeck, V. Water coordination and dehydration processes in defective UiO-66 type metal organic frameworks. *CrystEngComm* **2016**, *18* (37), 7056−7069.
(57) Caratelli, C.; Hajek, J.; Cirujano, F. G.; Waroquier, M.; Llabres i Xamena, F. X.; Van Speybroeck, V. Nature of active sites on UiO-66 and beneficial influence of water in the catalysis of Fischer esterification. *J. Catal.* **2017**, *352*, 401−414.
(58) Kattel, S.; Yan, B.; Chen, J. G.; Liu, P. CO2 hydrogenation on Pt, Pt/SiO2 and Pt/TiO2: Importance of synergy between Pt and oxide support. *J. Catal.* **2016**, *343*, 115−126.

https://dx.doi.org/10.1021/jacs.0c07153
J. Am. Chem. Soc. 2020, 142, 17105−17118